Optimization of Redox and Catalytic Performance of LaFeO$_3$ Perovskites: Synthesis and Physicochemical Properties

ANEES A. ANSARI [iD],[1,4,5] NAUSHAD AHMAD,[2] MANAWWER ALAM,[2]
SYED F. ADIL,[2] MOHAMED E. ASSAL,[2] ABDULRAHMAN ALBADRI,[3]
ABDULLAH M. AL-ENIZI,[2] and MUJEEB KHAN[2]

1.—King Abdullah Institute for Nanotechnology, King Saud University, Riyadh 11451, Saudi
Arabia. 2.—Department of Chemistry, College of Sciences, King Saud University, Riyadh 114551,
Saudi Arabia. 3.—National Center for Nanotechnology and Advanced Materials, King Abdulaziz
City for Science and Technology, Riyadh 11442, Saudi Arabia. 4.—e-mail: aneesaansari@gmail.
com. 5.—e-mail: amustaqeemahmad@ksu.edu.sa

La$_{1-x}$Ce$_x$FeO$_3$ perovskites were synthesized through a citric-acid assisted co-precipitation process. X-ray diffraction, transmission electron microscopy, energy dispersive x-ray analysis, thermogravimetric analysis, UV/Vis absorption spectroscopy, Fourier transform infrared spectroscopy, x-ray photoelectron spectroscopy, and an N$_2$-adsorption–desorption technique were applied for characterization of the perovskites. The x-ray analysis exhibited highly purified single-phase orthorhombic nanocrystals. The loading of Ce improved the specific surface area and affects the thermal stability along with the O$_2$ desorption characteristics. The BET analysis and textural characterization of a high concentration of the Ce-ion-doped LaFeO$_3$ perovskite revealed a relatively high specific surface area with respect to a low concentration of the doped perovskites, indicating the homogeneous dispersion of Ce ions within the crystal matrix. The oxidation states of trivalent La, Fe, O, and C in all perovskites were identified through an XPS study. The redox behavior was examined using temperature program reduction/oxidation techniques. The La$_{0.95}$Ce$_{0.05}$FeO$_3$ perovskites exhibited a high specific surface area and the best redox, catalytic, and reusability performances among the prepared catalysts, as revealed by the TPR/TPO, BET, and catalytic activity analyses.

Key words: LaFeO$_3$ perovskite, energy band gap, redox properties, textural properties

INTRODUCTION

Recently, the search for new energy storage technologies has sparked significant interest in catalytic applications. Catalysts are in great demand because they operate or oxidize under environmental conditions (temperature and pressure), and can convert volatile organic compounds into harmless compounds, thereby preserving eco-

systems.[1–3] Various types of catalysts based on semiconductor metal oxides,[4,5] mixed metal oxides,[6,7] noble metals,[8,9] transition metals,[5,10] zeolites, and perovskites[11–19] have been reported in the literature. Noble metals have been found to be particularly active for the oxidation of nitrous oxide. However, conventional noble metal catalysts are expensive, and their thermal stability is poor owing to sintering and metal loss in the form of volatile oxides. Perovskite oxides exhibit remarkable potential as an effective oxidation catalyst owing to their low cost, easy synthesis, and high thermal and chemical stability.[20] Because the high chemical stability of a perovskite structure allows the partial substitution of either La or M cation sites through

other metals with different oxidation states, perovskite oxides have been extensively studied as a catalyst material.[11,12,17–19] Lee et al. investigated the influence of K and Sr substitution in $LaMnO_3$ and $NdMnO_3$ perovskites on the surface properties and catalytic oxidation of ethane.[15,16] Feng et al. found good catalytic performance of K-doped three-dimensionally ordered macroporous $LaCoO_3$ perovskite.[21] Tabata et al. studied the electronic states of Cu-substituted $LaMnO_3$ perovskites through the XPS technique.[22] Wang et al. synthesized Co-substituted $LaMnO_3$ to investigate the oxygen storage capacity and catalytic activity of as-prepared perovskite.[23] Bedel et al. prepared different Co concentrations when substituting rhombohedral phase $LaFeO_3$ perovskites for a Fischer–Tropsch catalyst.[24] Peng et al. designed a Sr-substituted $LaMnO_3$ catalyst for NO_x storage and reduction.[25] In a similar report, researchers used Sr and Ce ions for doping into the $LaCoO_3$ perovskite catalysts for the combustion of methane.[26,27] Yoon et al. synthesized a silver-doped $LaMnO_3$ perovskite catalyst using a citric acid method for their use in the catalytic oxidation of NO.[28] Rousseau et al. observed that the doping of Sr and Co ions into a $LaFeO_3$ crystal matrix enhances the specific surface properties and alters the shape of the primary particles. These doped species activate the active sites of hydrocarbons.[11] Ciambelli et al. determined that the catalytic activity is affected by Sr ion substitution in a $SmMnO_3$ catalyst because of the fast reducibility of manganese ions.[18] Kumar et al. demonstrated that an appreciable increase in catalytic activity is observed in the doping of Ag and Ba ions into lanthanum magnate perovskite.[29] Fan et al. employed a Ag-supported $LaCoO_3$ perovskite for a catalytic oxidation of diesel soot particulates.[30] Onrubia et al. developed different Sr concentrations of doped $LaMnO_3$ and $LaCoO_3$ catalysts for efficient NO oxidation.[13] They observed that the Sr ions promote the textural and structural properties, and greatly improve the catalytic activity. Zhang et al. investigated the synergistic effects of Ca and Mg substitution in a $LaCoO_3$ catalyst on the crystal phase formation and catalytic performance.[31] In another report, Xue et al. measured that the doping of Ag ions into the $LaMnO_3$ perovskite matrix, causing a catalytic oxygen reduction reaction, is greatly improved owing to the improvement in the oxygen adsorption capacity.[32] In another similar report, Park et al., considered Ag-supported $LaMnO_3$ perovskite to be the best electrocatalyst for an oxygen reduction reaction.[8] In view of these published reports, we expected that the exchange of the A site with a similar valence and atomic size may partially distort the crystal matrix and enhance the oxygen vacancies. Owing to the distortion in the crystal lattice, the mobility of the oxygen species will improve to a considerable extent. Thus far, the partial change in concentration of La ions through a similar oxidation state and ionic radius

can disturb the valence of the perovskite matrix, generate oxygen vacancies, and enhance the mobility of surface-adsorbed lattice oxygen. Because of the addition of analogous valence metal, ions disrupt the crystal matrix and improve the perovskite stability resulting in an enhanced redox performance. In recent years, ceria has been used as a potential catalyst owing to its unique physicochemical properties, such as a cubic crystalline structure, transparency in visible regions, fast and reversible Ce^{4+}/Ce^{3+} redox cycles, stability within a wide range of temperature and pressures, and high oxygen storage/releasing capability.[33–35] The high mobility of oxygen vacancies plays a crucial role in any catalytic or electrochemical application, and has been extensively studied through both experimental and theoretical methods.[36,37] The addition of trivalent elements in the perovskite crystal matrix also causes the formation of O vacancies by replacing one Ce^{4+} ion for every two 3 + ions in the CeO_2 lattice. These vacancies increase the oxygen diffusion and thereby increase the ease with which the material can store and release oxygen. These excellent characteristics make them suitable catalysts for many different types of reactions, such as the oxidation of CO and hydrocarbons, and NO_x decomposition.

In this work, we synthesized $LaFeO_3$ perovskites loaded with different Ce ion concentration through a complex co-precipitation process. We systematically investigated the physicochemical properties and optimized the impact of Ce ion loading on the crystal structure, thermal stability, and optical, band gap, redox, and texture properties of the as-synthesized $LaFeO_3$ perovskites. The as-synthesized perovskites show a large surface area and display an excellent redox behavior under environmental conditions. Among the as-prepared perovskites, $La_{0.95}Ce_{0.05}FeO_3$ perovskites demonstrate a high specific surface area, and excellent redox and catalytic performances for the conversion of benzyl alcohol into benzaldehyde.

EXPERIMENTAL

Materials

$La(NO_3)_3 \cdot 7H_2O$ (BDH Chemicals, UK), $Ce(NO_3)_3 \cdot 6H_2O$ (BDH chemicals UK), $Fe(NO_3)_2 x H_2O$ (E-Merck, Germany), citric acid, and ammonia were used directly as received without further purification. Milli Q (Millipore, Bedford, USA) water was used for synthesis and characterization.

Synthesis of Different Ce Ion Doped $LaFeO_3$ Nanoparticles

Briefly, for the synthesis of $LaFeO_3$ perovskites, equal volumes of lanthanum nitrate and ferrous nitrate were dissolved separately in an equal volume of distilled water. This mixed solution was added to an aqueous dissolved citric acid with

constant mechanical stirring. Citric acid was used as a chelating agent for complexation with metal nitrates. The resulting mixed aqueous solution was magnetically stirred on a hot plate at 100°C until a homogeneous sol-like solution was formed. Later, an ammonia solution was quickly added to the complex mixture of precipitation. The occurring precipitate was separated through centrifugation and washed with distilled water and dried overnight in an oven at 100°C, followed by further annealing at 900°C in air for 3 h. A similar method was used for the preparation of different concentrations of cerium chloride hexahydrate (0.05 mol.%, 0.07 mol.%, and 0.10 mol.%) substituted $LaFeO_3$ nanoparticles.

Characterization

An x-ray diffraction pattern was carried out on a PANalytical X'PERT system (x-ray diffractometer) equipped with a Ni filter and using CuKα ($l = 1.5406$ Å). The surface morphology and chemical composition were obtained through field-emission transmission electron microscopy (FE-TEM) and energy dispersive x-ray (EDX) (JEM-2100F, JEOL, Japan) analysis operating at an accelerating voltage of 200 kV. The temperature program reduction (TPR) and temperature program oxygen (TPO) results were recorded from a Micromeritics Auto-Chem model 2910 equipped with a thermal conductivity detector. The textural properties of the catalysts were measured on a Micromeritics TriStar 3000 BET Analyzer, taking a value of 0.162 nm² for the cross-sectional area of the N_2 molecules adsorbed at 77 K. Powder samples were dried and degassed by heating gently to 90°C for 1 h, and then at 200°C for 3 h under flowing N_2 prior to the measurement. The free space in each sample tube was determined using He, which was assumed to avoid absorption. A thermogravimetric analysis (TGA) was measured (from TGA/DTA Mettler, Toledo, AG, Analytical CH-8603, Schwerzenbach, Switzerland). UV/Vis absorption spectra were recorded from a Perkin-Elmer Lambda-40 spectrophotometer within the range of 200–900 nm. Fourier transform infrared (FTIR) spectra were recorded from a Perkin–Elmer 580B IR spectrometer using the KBr pellet technique within the range of 4000–400 cm^{-1}.

Procedure for Aerobic Alcohol Oxidation

In a typical experiment, the oxidation of benzyl alcohol was carried out in a glass flask equipped with a magnetic stirrer, reflux condenser, and a thermometer. The mixture of benzyl alcohol (2 mmol), toluene (10 mL), and a catalyst (300 mg) was transferred in a glass three-necked round-bottomed flask (100 mL), and the resulting mixture was then heated to the desired temperature with vigorous stirring. The oxidation experiment was started by bubbling oxygen gas at a flow rate of

20 mL min^{-1} into the reaction mixture. After the reaction, the solid catalyst was filtered off by centrifugation, and the liquid products were analyzed using a gas chromatograph (GC, 7890A, Agilent Technologies, Inc.) equipped with a flame ionization detector (FID) and a 19019S-001 HP-PONA column to determine the conversion of alcohol and the product selectivity.

RESULTS AND DISCUSSION

As shown in Fig. 1, the x-ray diffraction pattern reveals most of the characteristic reflection lines observed at $2\theta = 22.88°$, $32.14°$, $39.74°$, $46.22°$, $52.14°$, $55.85°$, $57.52°$, $67.52°$, and $72.14°$, which correspond to the (012), (110), (104), (202), (024), (122), (116), (214), (018), (208), and (128) crystal planes, respectively. This indicates that as-synthesized perovskites are of a single phase with a highly purified orthorhombic phase (JCPDS card No. 084-0123) of $LaFeO_3$ perovskite.[12,38,39] The absence of any additional diffraction peaks related to iron oxide or ceria within the entire XRD range indicates the successful substitution and homogeneous distribution of Ce^{3+} ions inside the crystal lattice. The reflection bandwidth is significantly broadened in Ce^{3+} ion substituted perovskites as compared to the un-substituted $LaFeO_3$ perovskites (Fig. 1), which denotes the nanocrystalline size of the perovskite materials. In addition, the reflection peaks in the substituted perovskites are also slightly shifted toward higher 2θ angles upon increasing the Ce^{3+} ion substitution concentration, which is related to
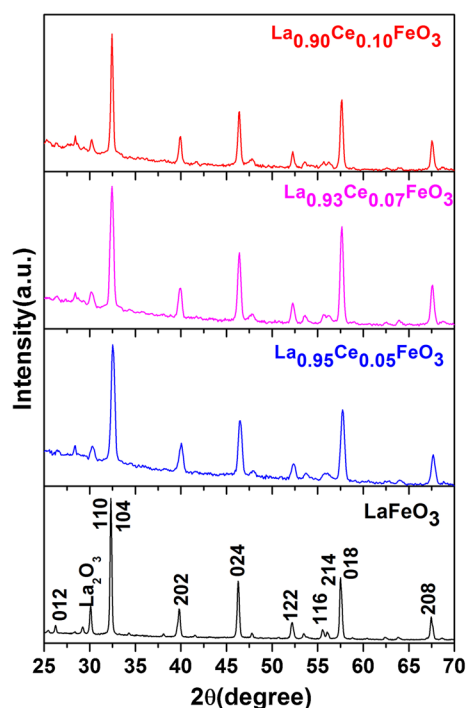

Fig. 1. X-ray diffraction pattern of $LaFeO_3$, $La_{0.95}Ce_{0.05}FeO_3$, $La_{0.93}Ce_{0.07}FeO_3$ and $La_{0.90}Ce_{0.10}FeO_3$ nanoparticles.

the substitution of Ce^{3+} ions of a smaller radius size in site A, causing a reduction in the interplanar distances in the crystal matrix.[24,40,41] The variations of the ionic size in the crystal matrix distort the crystal lattice, resulting in planes shifting toward a longer 2θ angle without altering the crystal structure.[42] A qualitative phase analysis proves the successful synthesis of highly purified single-phase $LaFeO_3$ and different Ce^{3+} ion substituted $LaFeO_3$ perovskites.

The TEM micrographs in Fig. 2a show the morphological structure of a Ce^{3+} ion substituted $La_{0.90}Ce_{0.10}FeO_3$ perovskite. TEM imaging shows irregular shape and size, and a smooth surface aggregated with an average size $\sim$ 100 nm particles that are well distributed. An energy dispersive x-ray (EDX) analysis illustrates the presence of expected metal contents in the as-prepared perovskite material. It is evident from the EDX spectrum that the elements La, Fe, Ce, and O are homogeneously distributed throughout the entire structure,
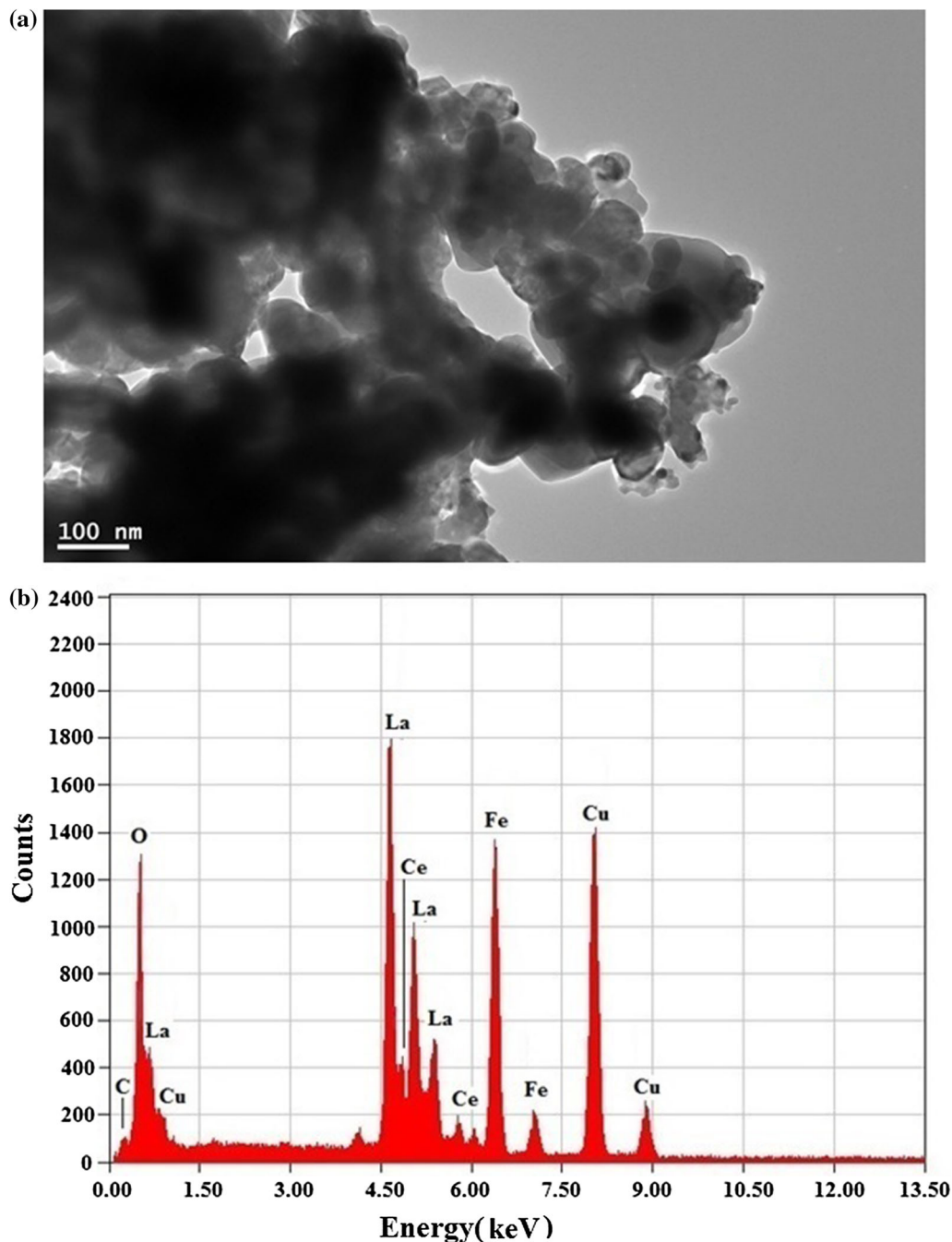

Fig. 2. (a) TEM image and (b) EDX spectrum of the $La_{0.90}Ce_{0.10}FeO_3$ nanoparticles.

suggesting that Ce ions are successfully substituted into the La$_{0.90}$Ce$_{0.10}$FeO$_3$ perovskite (Fig. 2b). The strong peaks of C and Cu observed belong to the carbon-coated copper grid.

The specific surface area, porosity, and pore size were examined through a BET analysis. The comparative BET-specific surface area results of the La$_{1-x}$Ce$_x$FeO$_3$ perovskite catalysts are summarized in Table I. The specific surface area results of the perovskites are relatively low at approximately 5.924–6.977 m^2 g^{-1}. Because all of these perovskite catalysts are dried at a higher temperature (900°C) for 3 h, the particles are highly aggregated (as shown in a TEM micrograph) causing a reduction in the surface area. In a comparative analysis, the La$_{0.93}$Ce$_{0.07}$FeO$_3$ perovskite catalyst revealed the lowest BET area (5.924 m^2 g^{-1}), whereas La$_{0.95}$Ce$_{0.05}$FeO$_3$ shows the highest surface area (6.977 m^2 g^{-1}).

A thermal analysis was conducted under a nitrogen atmosphere at 25–900°C with a heating rate of 10°C min^{-1}. As shown in Fig. 3, all thermograms demonstrate a similar decomposition pattern in all four samples. An initial weight loss of approximately 7.5 mol.% is observed at 50–400°C, which corresponds to the surface-attached physically adsorbed water molecules and organic moieties. Next, a sluggish weight loss was observed at 400–900°C, which is assigned to the removal of crystalline water attached in a different form with the oxide materials.[43–45] In general, two types of hydroxyl groups are known: the terminal group La-(OH), and bridge group La-(OH)-Fe. The decomposition temperatures of both surface-attached hydroxyl groups differ depending on their chemical bonding. We expected that the addition of small radius ceria into the perovskite matrix would shorten the bond distance, which is eliminated in a large amount (or burn) at low temperature. However, the weight loss observed at a higher temperature (700–900°C) is attributed to the combustion of carbon dioxide. FTIR spectra were recorded to investigate the surface chemistry of the as-synthesized perovskites (Fig. 4). A diffused infrared band and three strong intensity peaks located at 3440 cm^{-1}, 1470 cm^{-1}, and 1377 cm^{-1} are attributed to the stretching, bending, and scissoring vibrational modes of the hydroxyl (OH) groups, respectively, of the surface-attached water molecules.[43,45,46] These residual water molecules or surface hydroxyl groups were also detected through a TGA analysis. The strong intensity band of 700–400 cm^{-1} is assigned to the M-O stretching vibration mode, and reveals the formation of a metal–oxygen network within the perovskite material.[47]

Optical absorption spectra of pure LaFeO$_3$ and different Ce^{3+} ion substituted LaFeO$_3$ perovskite materials were measured within the UV/visible region to investigate the optical properties of the as-synthesized perovskite materials over the range of 300–900 nm. All of these perovskites exhibit
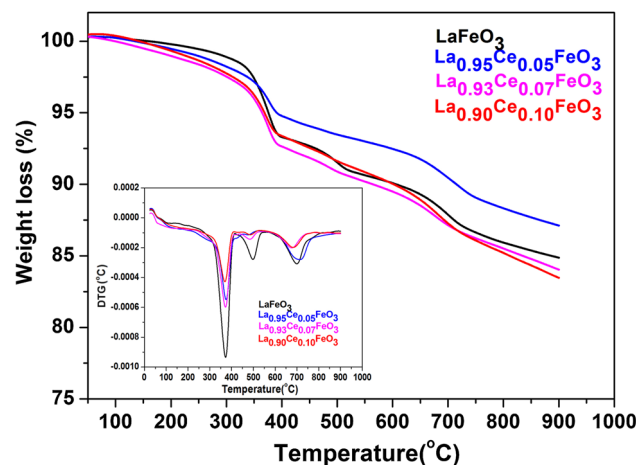

Fig. 3. Thermogravimetric analysis and an inset show the DTG curves of LaFeO$_3$, La$_{0.95}$Ce$_{0.05}$FeO$_3$, La$_{0.93}$Ce$_{0.07}$FeO$_3$ and La$_{0.90}$Ce$_{0.10}$FeO$_3$ nanoparticles.
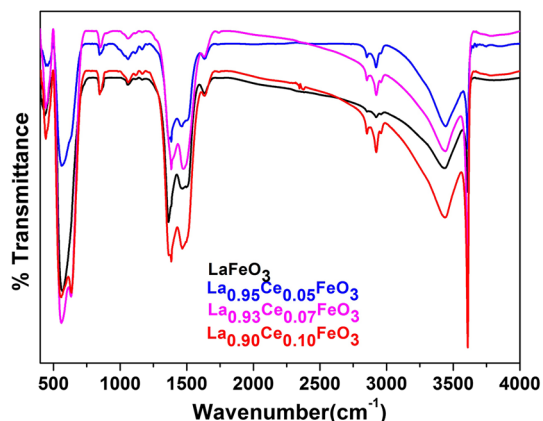
Fig. 4. FTIR spectra of LaFeO$_3$, La$_{0.95}$Ce$_{0.05}$FeO$_3$, La$_{0.93}$Ce$_{0.07}$FeO$_3$ and La$_{0.90}$Ce$_{0.10}$FeO$_3$ nanoparticles.

Table I. Single point surface area, BET surface area, pore size, pore volume La$_{1-x}$Ce$_x$FeO$_3$

Nominal composition	Single point BET (m^2 g^{-1})	Multi point BET (m^2 g^{-1})	Pore volume (cm^3 g^{-1})	Pore size (A)
LaFeO$_3$	5.729	6.208	0.001007	18.572
La$_{0.95}$Ce$_{0.05}$FeO$_3$	6.542	6.977	0.001065	18.730
La$_{0.93}$Ce$_{0.07}$FeO$_3$	5.463	5.924	0.000900	18.586
La$_{0.90}$Ce$_{0.10}$FeO$_3$	5.645	6.024	0.001036	18.626

strong absorption in the UV region, and the absorption extends to ∼ 700 nm (Fig. 5).[48] A broad high-intensity absorption band is observed within 300–700 nm, and in another weak intensity band with a peak maxima at 834 nm, which are attributed to the electron transitions from the valence band to the conduction band ($O_{2p} \rightarrow F_{3d}$).[12,42,49] The absorption spectral data are used to estimate the band gap energy (E_g) of the as-synthesized perovskites. The absorption data are fitted to the Tauc formulae to estimate the E_g values of the perovskites. The experimentally estimated E_g values for $LaFeO_3$, $La_{0.95}Ce_{0.05}FeO_3$, $La_{0.93}Ce_{0.07}FeO_3$, and $La_{0.90}Ce_{0.10}FeO_3$ perovskites are 1.18 eV, 1.32 eV, 1.34 eV, and 1.33 eV, respectively. As shown in Fig. 6, the E_g values are gradually increased with an increase in the substitution concentration of Ce^{3+} ions in the $LaFeO_3$ perovskite. The reason for the enhanced performance of Ce^{3+} ion substituted perovskites is due to the fact that the substitution of Ce^{3+} ions results in the formation of interstitial sites, which in turn create new energy levels (impurity energy levels) between the valence and conduction bands.[44,50] The impurity energy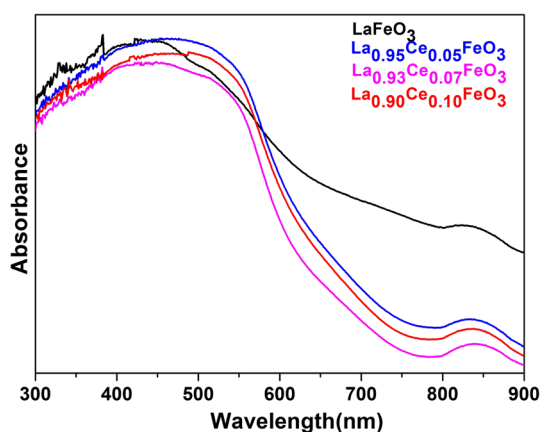 levels allow for an intrinsic band gap excitation under the visible light region. This implies that the higher energy state of 3d electrons from Ce^{3+}-cation dopants can be excited to the conduction band of $LaFeO_3$, thereby enhancing its catalytic performance. Similar values are within the range reported in the literature.[12,42,43,46,49]

A H_2-temperature program reduction (H_2-TPR) was employed to investigate the redox behavior of the unsubstituted $LaFeO_3$ and different concentrations of Ce^{3+}-ion substituted $LaFeO_3$ perovskites (Fig. 7). All samples display one major component with higher H_2 consumption within the temperature range of 100–800°C. A reduction peak is observed at a low temperature of ∼ 222°C with a small H_2 consumption, assigned to the reduction of Fe^{4+} to Fe^{3+}, which indicates the existence of trace amounts of Fe^{4+} ions in $LaFeO_3$ perovskite.[41,51] Next, the TPR profile of $LaFeO_3$ perovskite shows a major component at approximately 491°C along with two shoulders, the first at a low temperature of 433°C, and the second at a high temperature of 556°C,[24,41,52,53] which is attributed to the reduction of Fe^{3+} to Fe^{2+} and the surface chemisorbed bulk oxygen species. An observed small reduction peak at around 702°C assigned to the reduction of Fe^{2+} to metallic Fe^0,[52] which is assigned to the existence of small amount metallic Fe^0.[41,51,54] It is clear that La is not reducible under the current experimental conditions, and thus all of the observed peaks are assigned to the reduction of the Fe ions. A clear difference is observed upon the addition of various substitution concentrations of Ce^{3+} ions into the $LaFeO_3$ perovskite. It is worth noting that, upon increasing the amount of Ce^{3+} ions, the peak becomes stronger and the peak temperature shifts to a higher temperature from 491°C to 497°C, which corresponds to the consumption of adsorbed oxygen accompanied by the reduction of Fe^{4+} to Fe^{3+}, and the reduction of Ce^{4+} to Ce^{3+}.[40,41,52,54] It can be seen that a small shoulder also shifts or merges with the major reduction band, or significantly overlaps to form a broad reduction peak, indicating that the

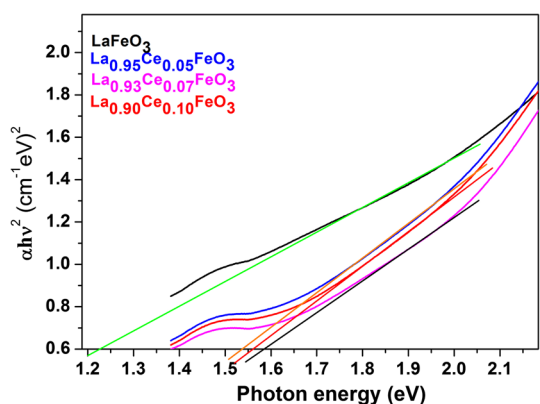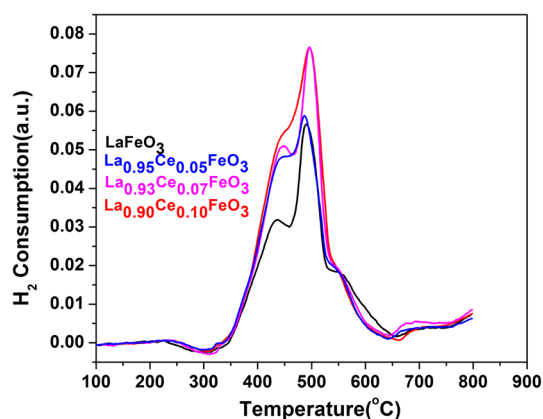Fig. 5. UV/Vis absorption spectra of $LaFeO_3$, $La_{0.95}Ce_{0.05}FeO_3$, $La_{0.93}Ce_{0.07}FeO_3$ and $La_{0.90}Ce_{0.10}FeO_3$ nanoparticles.

Fig. 6. The plot of $(\alpha h\nu)^2$ versus photon energy ($h\nu$) $LaFeO_3$, $La_{0.95}Ce_{0.05}FeO_3$, $La_{0.93}Ce_{0.07}FeO_3$ and $La_{0.90}Ce_{0.10}FeO_3$ nanoparticles.

Fig. 7. Temperature program reduction spectra of $LaFeO_3$, $La_{0.95}Ce_{0.05}FeO_3$, $La_{0.93}Ce_{0.07}FeO_3$ and $La_{0.90}Ce_{0.10}FeO_3$ nanoparticles.

subsurface lattice oxygen of the support may migrate to the surface and become an active oxygen species. In addition, the substituted Ce^{3+} ions are homogeneously dispersed inside the $LaFeO_3$ crystal matrix and significantly distort the M-O bond strength, which slightly diminishes the reduction of the surface chemisorption oxygen species.[52] Ceria is a well-known metal in the lanthanide series, and has a strong ability to reduce Ce^{4+} to Ce^{3+}.[33–35] However, the presence of ferrous ions in the crystal matrix simultaneously causes such a reduction. Based on the analysis results of H_2-TPR, we found that the redox properties of 10 mol.% Ce substituted ($La_{0.90}Ce_{0.10}FeO_3$ perovskite) catalysts are much better than those of pure $LaFeO_3$ and a smaller amount of Ce^{3+} substituted catalysts (Fig. 7). We expect that the chemical potential and reactivity of oxygen adjacent to the substituted metal cations will increase with an increase in the oxidation state and content of the substituted metal cations.[54] The high-quantity substitution of A-site cations and their interaction leads to the production of more hypervalent cations and a higher ratio of lattice oxygen vacancies, which weaken the M-O bonding strength.[21,52] Hence, they tend to lose much more lattice oxygen, i.e. more hypervalent metal cations can be easily reduced. It is also clear from the TGA results, as shown in Fig. 3, that upon increasing the additional amount of Ce ions into perovskite materials, the decomposition is increased owing to the weaker M-O bonding, which burns at low temperature. This may be the reason why high concentration Ce^{3+} substituted samples show a higher reducing ability in the middle of the H_2-TPR profile. However, the partially Ce^{3+} ion substituted samples are reduced from 4 + to 3 + owing to the loss of surrounding oxygen and the formation of oxygen vacancies.[54] This results in a lower lattice oxygen species ratio, a small amount of oxygen desorption, and a decrease in catalytic activity. According to the literature, reduction steps of Fe^{4+} to F^{3+} to Fe^{2+}, and Fe^0 occur in $LaFeO_3$ perovskite, the former at low

temperature with low hydrogen consumption, and the latter at high temperature with a similar low hydrogen consumption ratio.[41,48,51–53]

To determine the presence of various oxygen species, Fig. 8 demonstrates a temperature program oxidation (TPO) profile of the as-synthesized $LaFeO_3$, and $LaFeO_3$ perovskites with different amounts of Ce^{3+} ion substitution. Prolonged aging at 800°C was conducted to ensure the complete desorption of lattice oxygen species from the perovskite. As shown in Fig. 8, the TPO profile revealed a two-oxygen desorption region. A broad strong intensity oxygen desorption peak observed at a lower temperature (306°C) is assigned to the reverse transformation states of Fe^{2+} to Fe^{3+} along with the desorption of non-stoichiometric oxygen species, and the peak at a higher temperature (630°C) shows the chemisorption of Fe^{2+} to metallic Fe^0 in accordance with previous reports.[41,48,51–53] Moreover, upon increasing the amount of Ce ion substitution in $LaFeO_3$ perovskite, the oxygen desorption peak is shifted toward a lower temperature, and results in a remarkable enhancement in the integration area, which is highly consistent with the TGA results. These results suggest the enrichment of the perovskite surface owing to the existence of redox active ceria (Ce^{3+}/Ce^{4+}) ions. It is interesting to note that the Fe^{2+}/Fe^{3+} surface ratio is also enhanced following the ceria (Ce^{3+}/Ce^{4+}) ion enrichment (Fig. 8). This is probably attributable to the strong metal (Ce) support ($LaFeO_3$) interaction.
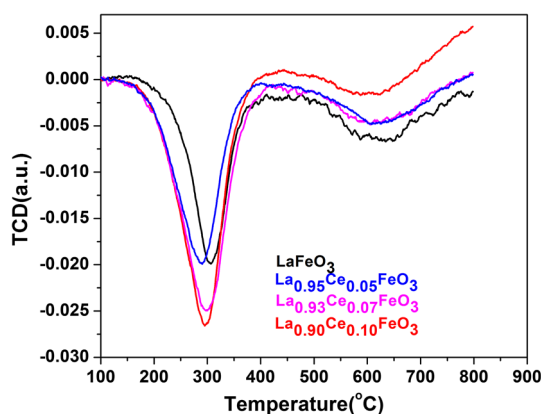

Fig. 8. Temperature program oxidation spectra of $LaFeO_3$, $La_{0.95}Ce_{0.05}FeO_3$, $La_{0.93}Ce_{0.07}FeO_3$ and $La_{0.90}Ce_{0.10}FeO_3$ nanoparticles.
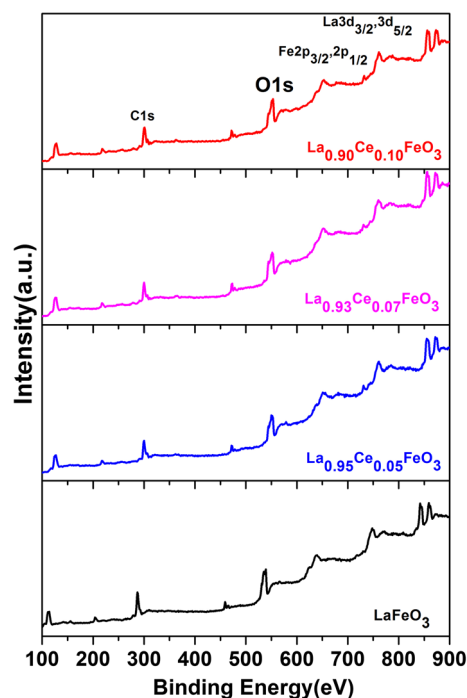

Fig. 9. XPS analysis of the La $3d_{3/2\&5/2}$ spectra recorded for the $LaFeO_3$, $La_{0.95}Ce_{0.05}FeO_3$, $La_{0.93}Ce_{0.07}FeO_3$ and $La_{0.90}Ce_{0.10}FeO_3$ nanoparticles.

An XPS analysis was conducted to investigate the chemical component in the different as-prepared Ce ion concentration doped $LaFeO_3$ perovskites. The surface composition and binding energies of La $3d_{5/2}$&$_{3/2}$, Fe $2p_{3/2}$&$_{1/2}$, O1s, and C1s were recorded using XPS for $LaFeO_3$ perovskites (Fig. 9).[55,56] All recorded peaks within the wide ranging spectra were calibrated using C1s (288.4 eV) as a Ref.[55]. As shown in Fig. 9, the La $3d$ transitions were observed to have two different contributions, located at 842 eV and 860 eV, along with the shake-up satellites. Fragmentation occurring in $3d$ peaks is due to the spin–orbit splitting of $3d_{5/2}$ (842 eV) and $3d_{3/2}$ (860 eV) ions, which are in oxide form. As shown in the wide and narrow ranging spectra in Figs. 9, 10 and 11, an observed broad peak at 712 along with some small intensity satellite peaks at 715 eV, 718 eV, and 720.6 eV, and at 723.6 eV, 725.7 eV, and 728.58 eV, are assigned to Fe$2p_{3/2}$ and Fe$2p_{1/2}$, respectively, as well as their satellite peaks, which are true fingerprints indicating the existence of different oxidation states of Fe$^{3+/2+}$ cations in the current perovskite oxide, as based on Fig. 10.[55] The XPS spectra of O1s in Fig. 11 show three peaks at binding energies of 524.4 eV, 529.95 eV, and 532 eV, which are ascribed to the lattice oxygen on the surface of perovskite (O_{latt}, La-O-La), a surface adsorbed oxygen species (O_{ads}, Fe-OH-La), and oxygen in molecular water adsorbed onto the perovskite surface (H-O-H), respectively.[56] As shown in Fig. 11, the mass percentage of the lattice (O_{latt}) and adsorbed oxygen (O_{ads}) is gradually increased

through an increase in the substitution concentration of Ce ions into the perovskite lattice (Fig. 11). The ratio of the lattice and adsorbed oxygen in $La_{0.90}aCe_{0.10}FeO_3$ is much higher than their respective non-Ce ion substituted perovskites. This suggests that the substitution of Ce ions is beneficial to the oxygen adsorption behavior of the perovskite catalyst. Furthermore, as shown in the TGA analysis results in Fig. 3, upon increasing the Ce ion substitution concentration in a perovskite lattice, the weight loss is increased at the same temperature, which could be due to the reduction of the large amount of oxygen species in crystalline form. These results are consistent with the TPR and TPO observations. We believe that small sized Ce ions in a perovskite lattice distort the crystal lattice, resulting in a reduction in the length of the bond, which is easily broken at low temperature. In previous studies, researchers observed that the high valency of iron species is highly preferable for redox properties over iron-based catalysts.[55,56] In addition, it can be clearly seen in the XPS spectra that the La$3d$, Fe $2p$, and O1s peaks greatly shift toward lower values upon an increase in the Ce ion concentrations, indicating the presence of a strong interaction between a La-O-Fe solid solution, which is inconsistent with the experimentally observed results. Most importantly, we were unable to observe the Ce ion peak in the current perovskite matrixes because the Ce ions in $LaCeFeO_3$ perovskites are mostly in a tetravalent state.[19]
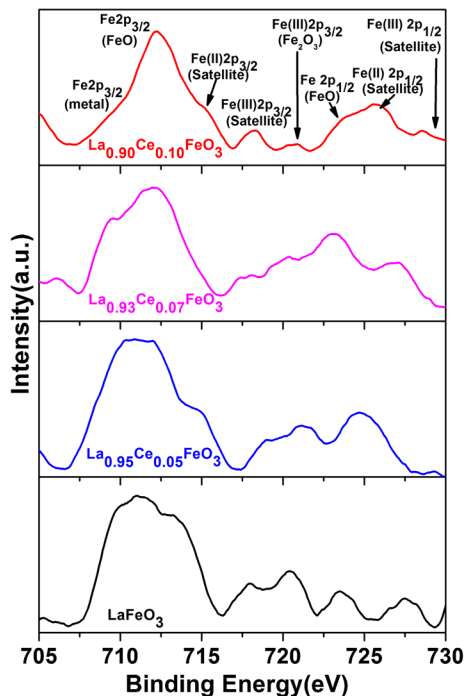

Fig. 10. XPS analysis of the Fe $2p_{1/2}$&$_{3/2}$ spectra recorded for the $LaFeO_3$, $La_{0.95}Ce_{0.05}FeO_3$, $La_{0.93}Ce_{0.07}FeO_3$ and $La_{0.90}Ce_{0.10}FeO_3$ nanoparticles.
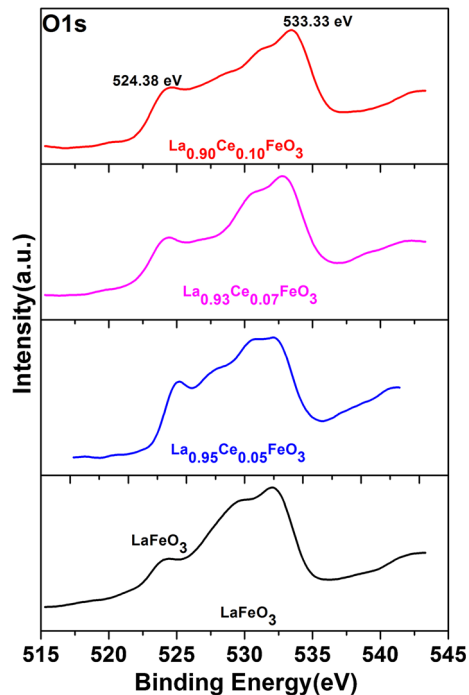

Fig. 11. XPS analysis of the O1s spectra recorded for the $LaFeO_3$, $La_{0.95}Ce_{0.05}FeO_3$, $La_{0.93}Ce_{0.07}FeO_3$ and $La_{0.90}Ce_{0.10}FeO_3$ nanoparticles.

Catalyst Recyclability

The as-prepared perovskites were tested for their catalytic properties as oxidation catalysts, and the oxidation of benzyl alcohol to aldehyde was studied. It was found that the un-doped perovskite, i.e. LaFeO$_3$, starts off with a conversion product of 7% within 2 h; however, when the reaction was continued for 12 h more, the conversion product yield increased 17.8%. It is worth noting that, upon the substitution of trivalent Ce in perovskite, a significant enhancement (18% conversion yield) in the catalytic performance was measured. On the other hand, upon further increase in the Ce ion substitution concentration in a perovskite lattice, the conversion yield was gradually diminished by 5.4% and 4.3% for La$_{0.93}$Ce$_{0.07}$FeO$_3$ and La$_{0.90}$Ce$_{0.10}$FeO$_3$ perovskites, respectively. Upon further increase, the reaction yielded a 15% and 13% conversion product within a 12-h reaction time, indicating that the Ce atoms in the perovskite hinder the active site of the perovskite, leading to a depreciation of the catalytic performance. Furthermore, the selectivity toward benzaldehyde was found to be > 99% in all cases. Figure 12 shows the results of a kinetic study of all catalysts. Comparing the catalytic performance with the surface area for a better understanding of the catalytic efficiency of the as-synthesized perovskites, it can be seen that the surface area of LaFeO$_3$ was approximately 6.2 m^2 g^{-1}, whereas after inclusion of 5 mol.% Ce^{3+} ions in the perovskite lattice, the specific surface area of the catalyst was significantly improved by 12%, i.e. 6.97 m^2 g^{-1}. However, only a mild improvement in the catalytic activity was observed, whereas the
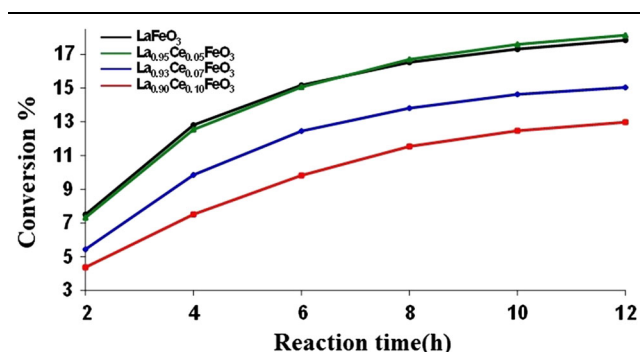
specific activity of both perovskite catalysts was found to be 0.15 mmol g^{-1} h^{-1}. Furthermore, upon increasing the Ce^{3+} substitution concentration by 7 mol.% and 10 mol.%, a drastic decrease in the specific surface area was observed, resulting in a decreased catalytic performance, which indicates that Ce ions block the active sites in the perovskites. The specific activity of the catalysts decreased to 0.13 mmol g^{-1} h^{-1} and 0.11 mmol g^{-1} h^{-1} for the catalysts La$_{0.93}$Ce$_{0.07}$FeO$_3$ and La$_{0.90}$Ce$_{0.10}$FeO$_3$, respectively. The number of turnovers and the turnover frequency of the catalyst were calculated, and the values obtained are shown in Fig. 12. In a comparative analysis, La$_{0.95}$Ce$_{0.05}$FeO$_3$ demonstrated the highest TON and TOF values among all of the catalysts (Table II). It can be concluded that the substitution of Ce^{3+} in the perovskite system alters the specific surface area, resulting in an enhanced catalytic performance. However, upon increasing the percentage of Ce^{3+} ion substitution, a slight reduction in the catalytic performance was observed. Among all of the perovskites, the La$_{0.95}$Ce$_{0.05}$FeO$_3$ catalyst provides a high conversion yield, which indicates a good catalytic performance along with their reusability. The catalyst was used several times, and it was found that the catalytic performance depreciated by 0.57% for the first reuse (Fig. 13). Furthermore, the reusability of the perovskites leads to an additional loss of catalytic activity, and upon four reuses, the catalyst yielded a 12.7% conversion product after a 12 h reaction time. The catalyst recovery has considerable importance from both industrial and academic perspectives. The recyclability of La$_{0.95}$Ce$_{0.05}$FeO$_3$ for the selective oxidation of benzyl alcohol through molecular oxygen was studied under optimized circumstances. To examine the reusability and stability of the as-synthesized catalyst after completion of the reaction, the toluene was evaporated, and fresh toluene (solvent) was added. The mixture was then filtered through a simple filtration to recover the catalyst. The filtered catalyst was washed sequentially with toluene and dried at 100°C for 12 h.

CONCLUSIONS

La$_{1-x}$Ce$_x$FeO$_3$ nanocrystals were successfully prepared using a co-precipitation method at a relatively low temperature, and various physicochemical techniques were characterized. The absence of ceria

Fig. 12. Graphical representation of the kinetics of oxidation of benzyl alcohol to benzaldehyde employing perovskites.

Table II. Aerobic oxidation of benzyl alcohol employing La$_{1-x}$Ce$_x$FeO$_3$ catalysts

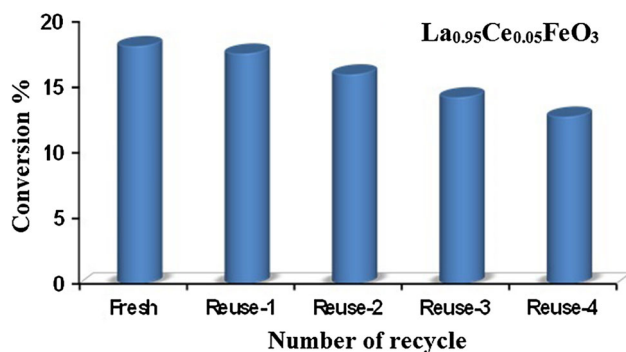| Entry	Catalyst	Conv. (%)	Sel. (%)	Specific activity (mmol g^{-1} h^{-1})	TON	TOF (h^{-1})
1	LaFeO$_3$	17.84	> 99	0.15	–	–
2	La$_{0.95}$Ce$_{0.05}$FeO$_3$	18.13	> 99	0.15	508.06	42.34
3	La$_{0.93}$Ce$_{0.07}$FeO$_3$	15.04	> 99	0.13	301.04	25.09
4	La$_{0.90}$Ce$_{0.10}$FeO$_3$	12.98	> 99	0.11	181.92	15.16

Fig. 13. Recyclability of $La_{0.95}Ce_{0.05}FeO_3$ for the aerial oxidation of benzyl alcohol. (Reaction conditions: 2 mmol of 1-benzyl alcohol, calcination temperature at 300°C, oxygen with rate 20 mL min^{-1}, 0.3 g of catalyst, 10 mL of toluene, reaction temperature at 100°C, and 12 h of reaction time).

peaks in the XRD pattern infers the homogeneous distribution of Ce ions within the perovskite crystal lattice. Differences in the energy band gap, thermal decomposition, and altered redox behavior occurred owing to the doping of small sized Ce ions interrupting the crystal lattice. An XPS analysis revealed the existence of large amounts of electrophilic oxygen species, which are able to activate the hydrocarbons. In a comparative study, we observed that the Ce ion doping in $LaFeO_3$ perovskite reinforces the interaction between La-O-Ce and Ce-O-Fe, thereby leading to an enhanced reduction capability, which improves the catalytic activity. A homogeneous distribution of Ce ions in $LaFeO_3$ perovskite allowed more Ce atoms to reside on the crystal surface, and simultaneously reserved more of the Ce component in the catalyst. It can be concluded that the inclusion of Ce^{3+} in the perovskite system has no positive effect on its performance as an oxidation catalyst. In a comparative analysis, a $La_{0.95}Ce_{0.05}FeO_3$ catalyst provided a good texture, and a high redox and catalytic performance, toward benzyl alcohol oxidation with excellent selectivity and reusability with respect to undoped $LaFeO_3$ and high-quantity doped $La_{0.93}Ce_{0.07}FeO_3$ and $La_{0.90}Ce_{0.10}FeO_3$ perovskite catalysts. Further modifications and studies can help ascertain the optimum percentage of Ce^{3+} toward the enhancement of the catalytic performance. The results of this newly developed strategy are highly promising for the construction of other binary metal nanoparticles with large active areas of different types of catalytic applications.

ACKNOWLEDGMENTS

REFERENCES

1. W.J. Xu, F.L. Lyu, Y.C. Bai, A.Q. Gao, J. Feng, Z.X. Cai, and Y.D. Yin, *Nano Energy* 43, 110 (2018).
2. H.B. Huang, Y. Xu, Q.Y. Feng, and D.Y.C. Leung, *Catal. Sci. Technol.* 5, 2649 (2015).
3. S. Chaturvedi, P.N. Dave, and N.K. Shah, *J. Saudi Chem. Soc.* 16, 307 (2012).
4. X.J. Wen, C.G. Niu, L. Zhang, C. Liang, and G.M. Zeng, *Appl. Catal. B Environ.* 221, 701 (2018).
5. J.Y. Luo, M. Meng, J.S. Yao, X.G. Li, Y.Q. Zha, X. Wang, and T.Y. Zhang, *Appl. Catal. B Environ.* 87, 92 (2009).
6. S. Khamarui, Y. Saima, R.M. Laha, S. Ghosh, and D.K. Maiti, *Sci. Rep. Uk* 5, 8636 (2015).
7. X. Liang, X. Wang, Y. Zhuang, B. Xu, S.M. Kuang, and Y.D. Li, *J. Am. Chem. Soc.* 130, 2736 (2008).
8. S.A. Park, E.K. Lee, H. Song, and Y.T. Kim, *Sci. Rep. Uk* 5, 13552 (2015).
9. Q. Fu, W.L. Deng, H. Saltsburg, and M. Flytzani-Stephanopoulos, *Appl. Catal. B. Environ.* 56, 57 (2005).
10. Y.Y. Huang, T.S. Zhao, G. Zhao, X.H. Yan, and K. Xu, *J. Power Sources* 304, 74 (2016).
11. S. Rousseau, S. Loridant, P. Delichere, A. Boreave, J.P. Deloume, and P. Vernoux, *Appl. Catal. B. Environ.* 88, 438 (2009).
12. Q. Peng, B. Shan, Y.W. Wen, and R. Chen, *Int. J. Hydrogen Energy* 40, 15423 (2015).
13. J.A. Onrubia, B. Pereda-Ayo, U. De-La-Torre, and J.R. Gonzalez-Velasco, *Appl. Catal. B Environ.* 213, 198 (2017).
14. M.J. Martinez-Lope, J.A. Alonso, M. Retuerto, and M.T. Fernandez-Diaz, *Inorg. Chem.* 47, 2634 (2008).
15. Y.N. Lee, R.M. Lago, J.L.G. Fierro, and J. Gonzalez, *Appl. Catal. A Gen.* 215, 245 (2001).
16. Y.N. Lee, R.M. Lago, J.L.G. Fierro, V. Cortes, F. Sapina, and E. Martinez, *Appl. Catal. A Gen.* 207, 17 (2001).
17. P. Ciambelli, S. Cimino, S. De Rossi, L. Lisi, G. Minelli, P. Porta, and G. Russo, *Appl. Catal. B Environ.* 29, 239 (2001).
18. P. Ciambelli, S. Cimino, S. De Rossi, M. Faticanti, L. Lisi, G. Minelli, I. Pettiti, P. Porta, G. Russo, and M. Turco, *Appl. Catal. B Environ.* 24, 243 (2000).
19. S. Ben Hammouda, F.P. Zhao, Z. Safaei, I. Babu, D.L. Ramasamy, and M. Sillanpaa, *Appl. Catal. B Environ.* 218, 119 (2017).
20. H. Pan, *Renew. Sust. Energy Rev.* 57, 584 (2016).
21. N.J. Feng, C. Chen, J. Meng, Y. Wu, G. Liu, L. Wang, H. Wan, and G.F. Guan, *Catal. Sci. Technol.* 6, 7718 (2016).
22. K. Tabata, Y. Hirano, and E. Suzuki, *Appl. Catal. A Gen.* 170, 245 (1998).
23. J. Wang, Y.G. Su, X.Q. Wang, J.H. Chen, Z. Zhao, and M.Q. Shen, *Catal. Commun.* 25, 106 (2012).
24. L. Bedel, A.C. Roger, C. Estournes, and A. Kiennemann, *Catal. Today* 85, 207 (2003).
25. Y. Peng, W.Z. Si, J.H. Li, J. Crittenden, and J.M. Hao, *Catal. Sci. Technol.* 5, 2478 (2015).
26. M. Alifanti, J. Kirchnerova, and B. Delmon, *Appl. Catal. A Gen.* 245, 231 (2003).
27. C.Q. Chen, W. Li, C.Y. Cao, and W.G. Song, *J. Mater. Chem.* 20, 6968 (2010).
28. D.Y. Yoon, E. Lim, Y.J. Kim, J.H. Kim, T. Ryu, S. Lee, B.K. Cho, I.S. Nam, J.W. Choung, and S. Yoo, *J. Catal.* 319, 182 (2014).
29. S. Kumar, Y. Teraoka, A.G. Joshi, S. Rayalu, and N. Labhsetwar, *J. Mol. Catal. A Chem.* 348, 42 (2011).
30. Q. Fan, S. Zhang, L.Y. Sun, X. Dong, L.C. Zhang, W.J. Shan, and Z.M. Zhu, *Chin. J. Catal.* 37, 428 (2016).
31. J.Y. Zhang, D.D. Tan, Q.J. Meng, X.L. Weng, and Z.B. Wu, *Appl. Catal. B. Environ.* 172, 18 (2015).
32. Y.J. Xue, H. Miao, S.S. Sun, Q. Wang, S.H. Li, and Z.P. Liu, *RSC Adv.* 7, 5214 (2017).
33. A.A. Ansari, P.R. Solanki, and B.D. Malhotra, *Appl. Phys. Lett.* 92, 263901 (2008).
34. A.A. Ansari, A. Kaushik, P.R. Solanki, and B.D. Malhotra, *Electrochem. Commun.* 10, 1246 (2008).

35. S. Patil, S. Seal, Y. Guo, A. Schulte, and J. Norwood, *Appl. Phys. Lett.* 88, 243110 (2006).
36. P.R. Solanki, C. Dhand, A. Kaushik, A.A. Ansari, K.N. Sood, and B.D. Malhotra, *Sens. Actuators B Chem.* 141, 551 (2009).
37. A. Kaushik, P.R. Solanki, A.A. Ansari, S. Ahmad, and B.D. Malhotra, *Nanotechnology* 20, 055105 (2009).
38. H. Arandiyan, H.X. Dai, J.G. Deng, Y.X. Liu, B.Y. Bai, Y. Wang, X.W. Li, S.H. Xie, and J.H. Li, *J. Catal.* 307, 327 (2013).
39. J.T. Mefford, W.G. Hardin, S. Dai, K.P. Johnston, and K.J. Stevenson, *Nat. Mater.* 13, 726 (2014).
40. K. Zhao, F. He, Z. Huang, G.Q. Wei, A.Q. Zheng, H.B. Li, and Z.L. Zhao, *Appl. Energy* 168, 193 (2016).
41. P. Ciambelli, S. Cimino, L. Lisi, M. Faticanti, G. Minelli, I. Pettiti, and P. Porta, *Appl. Catal. B Environ.* 33, 193 (2001).
42. C. Sasikala, N. Durairaj, I. Baskaran, B. Sathyaseelan, M. Henini, and E. Manikandan, *J. Alloys Compd.* 712, 870 (2017).
43. A.A. Ansari, J. Labis, M. Alam, S.M. Ramay, N. Ahmad, and A. Mahmood, *Phase Transit.* 89, 261 (2016).
44. A.A. Ansari, J. Labis, M. Alam, S.M. Ramay, N. Ahmad, and A. Mahmood, *J. Chin. Chem. Soc. Taip* 62, 925 (2015).
45. A.A. Ansari, J. Labis, M. Alam, S.M. Ramay, N. Ahmad, and A. Mahmood, *J. Electroceram.* 36, 150 (2016).
46. A.A. Ansari, J.P. Labis, M. Alam, S.M. Ramay, N. Ahmad, and A. Mahmood, *Acta Metall. Sin. Engl.* 29, 265 (2016).
47. A.A. Ansari, M. Alam, J.P. Labis, S.A. Alrokayan, G. Shafi, T.N. Hasan, N.A. Syed, and A.A. Alshatwi, *J. Mater. Chem.* 21, 19310 (2011).
48. S. Thirumalairajan, K. Girija, I. Ganesh, D. Mangalaraj, C. Viswanathan, A. Balamurugan, and N. Ponpandian, *Chem. Eng. J.* 209, 420 (2012).
49. G. Iervolino, V. Vaiano, D. Sannino, L. Rizzo, and P. Ciambelli, *Int. J. Hydrogen Energy* 41, 959 (2016).
50. A.A. Saad, W. Khan, P. Dhiman, A.H. Naqvi, and M. Singh, *Electron. Mater. Lett.* 9, 77 (2013).
51. X.J. Zhang, H.J. Li, Y. Li, and W.J. Shen, *Chin. J Catal.* 33, 1109 (2012).
52. Y.C. Wei, Z. Zhao, J.Q. Jiao, J. Liu, A.J. Duan, and G.Y. Jiang, *Catal. Today* 245, 37 (2015).
53. M.A. Soria, P. Perez, S.A.C. Carabineiro, F.J. Maldonado-Hodar, A. Mendes, and L.M. Madeira, *Appl. Catal. A Gen.* 470, 45 (2014).
54. Z.Y. Zhong, K.D. Chen, Y. Ji, and Q.J. Yan, *Appl. Catal. A Gen.* 156, 29 (1997).
55. S. Thirumalairajan, K. Girija, V.R. Mastelaro, V. Ganesh, and N. Ponpandian, *RSC Adv.* 4, 25957 (2014).
56. S. Thirumalairajan, K. Girija, N.Y. Hebalkar, D. Mangalaraj, C. Viswanathan, and N. Ponpandian, *RSC Adv.* 3, 7549 (2013).